Supplementary information for:
Proposal to Test Quantum Wave-Particle Superposition on Massive Mechanical Resonators

Wei Qin,[1,2] Adam Miranowicz,[1,3] Guilu Long,[4] J. Q. You,[5,2] and Franco Nori[1,6]

[1] Theoretical Quantum Physics Laboratory, RIKEN Cluster for Pioneering Research, Wako-shi, Saitama 351-0198, Japan
[2] Quantum Physics and Quantum Information Division,
Beijing Computational Science Research Center, Beijing 100193, China
[3] Faculty of Physics, Adam Mickiewicz University, 61-614 Poznań, Poland
[4] State Key Laboratory of Low-Dimensional Quantum Physics and
Department of Physics, Tsinghua University, Beijing 100084, China
[5] Department of Physics and State Key Laboratory of Modern Optical
Instrumentation, Zhejiang University, Hangzhou 310027, China
[6] Department of Physics, The University of Michigan, Ann Arbor, Michigan 48109-1040, USA

Here, we, first, in Sec. I present more details of how to obtain the spin-controlled coherent coupling between separated mechanical resonators. Second, in Sec. II, we show the detailed implementation of the controlled Hadamard gate, the phase gate, and the mechanical quantum delayed-choice experiment. Next, in Sec. III, we derive in detail the phonon occupation of each CNT at finite temperatures. Then, Sec. IV describes the detailed derivation of the fluctuation noise and the detailed analysis of the requirement of resolving the coherent signal from the environment-induced fluctuation. Finally, in Sec. V we show the method of the numerical simulation used in this work.

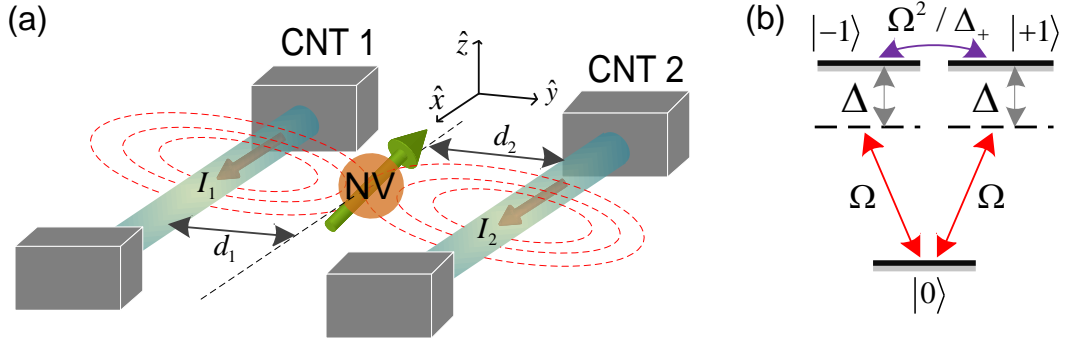## I. Spin-controlled coherent coupling between separated mechanical resonators

FIG. 1. (Color online) (a) Schematic representation of a mechanical quantum delayed-choice experiment with an NV electronic spin and two carbon nanotubes (CNTs). The mechanical vibrations of the CNTs, labelled by $k = 1, 2$, are completely decoupled or coherently coupled, depending, respectively, on whether or not the intermediate spin is in the spin state $|0\rangle$, with the dc current I_k through the kth CNT, and the distance d_k between the spin and the kth CNT. (b) Level structure of the driven NV spin in the electronic ground state. Here we have assumed that the Zeeman splitting between the spin states $|\pm 1\rangle$ is eliminated by applying an external field.

The effective Hamiltonian H_{eff} in the article describes a spin-mediated CNT-CNT coupling conditioned on the NV spin state. This is the basic element underlying our proposal. To understand more explicitly the spin-controlled coupling between the CNTs, in this section we derive in detail the effective Hamiltonian. We consider a hybrid quantum system consisting of two parallel CNTs and an NV electronic spin (a qutrit), as depicted in Fig. 1(a). Here, for convenience, illustrations in Figs. 1(b) and 1(c) in the article are reproduced in Figs. 1(b) and 1(a), respectively. The CNTs, respectively, carry dc currents I_1 and I_2, both along the $+\hat{x}$–direction. A spin is placed between them, at a distance d_1 (d_2) from the first (second) CNT. According to the Biot-Savart law, the CNTs can, at the position of the spin, generate a magnetic field $\vec{B}_{\text{cnt}}^{(0)} = B_{\text{cnt}}^{(0)} \hat{z}$, where

$$B_{\text{cnt}}^{(0)} = \sum_{k=1,2} (-1)^{k-1} \frac{\mu_0 I_k}{2\pi d_k},$$

(1)

$\hat{\epsilon}$ ($\epsilon = x, y, z$) is a unit vector in the $\hat{\epsilon}$–direction, μ_0 is the vacuum permeability, and the subscript "cnt" refers to the CNTs. When the CNTs vibrate along the $\hat{y}$–direction, the magnetic field is parametrically modulated by their mechanical displacements y_1 and y_2, and then is reexpressed, up to first order, as $\vec{B}_{\mathrm{cnt}} = \vec{B}_{\mathrm{cnt}}^{(0)} + \vec{B}_{\mathrm{cnt}}^{(1)}$, where $\vec{B}_{\mathrm{cnt}}^{(1)} = B_{\mathrm{cnt}}^{(1)}\hat{z}$ is a first-order modification, and where $B_{\mathrm{cnt}}^{(1)} = \sum_{k=1,2} G_k y_k$, with a magnetic-field gradient,

$$G_k = \frac{\mu_0 I_k}{2\pi d_k^2}. \tag{2}$$

Note that, here, $y_1 > 0$ ($y_2 < 0$) indicates a decrease in d_1 (d_2). Therefore, the sign, $(-1)^{k-1}$, in Eq. (1) does not appear in Eq. (2). Furthermore, an external magnetic field, $\vec{B}_{\mathrm{ext}} = B_x(t)\hat{x} + B_z\hat{z}$, is applied to the NV spin. We have assumed, as required below, that $B_x(t)$ is a time-dependent component but B_z is a dc component. The Hamiltonian governing the NV spin is therefore given by

$$H_{\mathrm{NV}} = \hbar D S_z^2 + \mu_B g_s \left[B_{\mathrm{cnt}}^{(0)} + B_z \right] S_z + \mu_B g_s B_x(t) S_x + \mu_B g_s B_{\mathrm{cnt}}^{(1)} S_z, \tag{3}$$

where $g_s \simeq 2$ is the Landé factor, μ_B the Bohr magneton, $D \simeq 2\pi \times 2.87$ GHz the zero-field splitting, and S_ϵ the ϵ–component of the spin operator $\vec{S}$ ($\epsilon = x, y, z$). In terms of the eigenstates, $\{|m_s\rangle, m_s = 0, \pm 1\}$, of S_z, the operator S_ϵ is expanded as

$$S_x = \frac{1}{2}\begin{pmatrix} 0 & \sqrt{2} & 0 \\ \sqrt{2} & 0 & \sqrt{2} \\ 0 & \sqrt{2} & 0 \end{pmatrix}, \ S_y = \frac{1}{2i}\begin{pmatrix} 0 & \sqrt{2} & 0 \\ -\sqrt{2} & 0 & \sqrt{2} \\ 0 & -\sqrt{2} & 0 \end{pmatrix}, \ \text{and} \ S_z = \frac{1}{2}\begin{pmatrix} +1 & 0 & 0 \\ 0 & 0 & 0 \\ 0 & 0 & -1 \end{pmatrix}, \tag{4}$$

and accordingly, the Hamiltonian H_{NV} is transformed to

$$\begin{aligned} H_{\mathrm{NV}} = {} & \left\{ \hbar D + \mu_B g_s \left[B_{\mathrm{cnt}}^{(0)} + B_z \right] \right\} |+1\rangle\langle+1| + \left\{ \hbar D - \mu_B g_s \left[B_{\mathrm{cnt}}^{(0)} + B_z \right] \right\} |-1\rangle\langle-1| \\ & + \frac{1}{\sqrt{2}} \mu_B g_s B_x(t) \left(|-1\rangle\langle 0| + |+1\rangle\langle 0| + \mathrm{H.c.} \right) \\ & + \mu_B g_s B_{\mathrm{cnt}}^{(1)} \left(|+1\rangle\langle+1| - |-1\rangle\langle-1| \right). \end{aligned} \tag{5}$$

We find that the magnetic field along the $\hat{z}$–direction causes different Zeeman shifts to be imposed, respectively, on the spin states $|\pm 1\rangle$, and also that the magnetic field along the $\hat{x}$–direction drives the transition between the spin states $|0\rangle$ and $|\pm 1\rangle$.

The quantum treatment of the mechanical motion demonstrates that the mechanical vibrations of the CNTs can be modelled by two single-mode harmonic oscillators with a Hamiltonian

$$H_{\mathrm{mv}} = \sum_{k=1,2} \hbar \omega_k b_k^\dagger b_k, \tag{6}$$

where ω_k is the phonon frequency and b_k ($b_k^\dagger$) is the phonon annihilation (creation) operator. Here, we have subtracted the constant zero-point energy $\hbar\omega_k/2$. The mechanical displacement y_k is accordingly expressed as

$$y_k = y_{\mathrm{zp}}^{(k)} \left(b_k + b_k^\dagger \right) \equiv y_{\mathrm{zp}}^{(k)} q_k, \tag{7}$$

where q_k is the canonical phonon position operator, and $y_{\mathrm{zp}}^{(k)} = [\hbar / (2m_k \omega_k)]^{1/2}$, with m_k being the effective mass, describes the zero-point (zp) motion. Combining Eqs. (5), (6), and (7) gives the full Hamiltonian of the hybrid system,

$$\begin{aligned} H_F = {} & \sum_{k=1,2} \hbar \omega_k b_k^\dagger b_k + \left\{ \hbar D + \mu_B g_s \left[B_{\mathrm{cnt}}^{(0)} + B_z \right] \right\} |+1\rangle\langle+1| \\ & + \left\{ \hbar D - \mu_B g_s \left[B_{\mathrm{cnt}}^{(0)} + B_z \right] \right\} |-1\rangle\langle-1| \\ & + \frac{1}{\sqrt{2}} \mu_B g_s B_x(t) \left(|-1\rangle\langle 0| + |+1\rangle\langle 0| + \mathrm{H.c.} \right) \\ & + \sum_{k=1,2} \mu_B g_s G_k y_{\mathrm{zp}}^{(k)} \left(|+1\rangle\langle+1| - |-1\rangle\langle-1| \right) q_k. \end{aligned} \tag{8}$$

The last line in Eq. (8) describes a magnetic coupling between the spin and the mechanical modes. In order to realize a tunable detuning between them, $B_x(t)$ is chosen to be $B_x(t) = B_0 \cos(\omega_0 t)$ with amplitude B_0 and frequency ω_0. In a frame rotating at $H_{\rm rot} = \hbar\omega_0(|-1\rangle\langle-1| + |+1\rangle\langle+1|)$, the full Hamiltonian can be divided into two parts, $H_F = H_{\rm low} + H_{\rm high}$, where

$$H_{\rm low} = \sum_{k=1,2} \hbar\omega_k b_k^\dagger b_k + \hbar\delta_+ |+1\rangle\langle+1| + \hbar\delta_- |-1\rangle\langle-1|$$
$$+ \hbar\Omega(|-1\rangle\langle0| + |+1\rangle\langle0| + {\rm H.c.})$$
$$+ \sum_{k=1,2} \hbar g_k (|+1\rangle\langle+1| - |-1\rangle\langle-1|) q_k, \tag{9}$$

$$H_{\rm high} = \hbar\Omega\left[\exp(i2\omega_0 t)|-1\rangle\langle0| + \exp(i2\omega_0 t)|+1\rangle\langle0| + {\rm H.c.}\right], \tag{10}$$

account for the low- and high-frequency components, respectively. Here, we have defined

$$\hbar\delta_\pm = \hbar D \pm \mu_B g_s \left[B_{\rm nt}^{(0)} + B_z\right] - \hbar\omega_0,$$
$$\hbar\Omega = \frac{1}{2\sqrt{2}}\mu_B g_s B_0,$$
$$\hbar g_k = \mu_B g_s G_k y_{\rm zp}^{(k)}. \tag{11}$$

Roughly, having $\delta_\pm' = \delta_\pm + 2\omega_0 \gg \Omega$ allows one to make the rotating-wave approximation (RWA), and to straightforwardly remove $H_{\rm high}$. However, as demonstrated in Sec. V, the accumulated error increases during the evolution, causing the dynamics driven by $H_{\rm low}$ to deviate largely from that driven by H_F. Thus, we are *not* using the RWA here. In order to suppress the error accumulation, we need to analyze the effects of $H_{\rm high}$ in the limit $\delta_\pm' \gg \Omega$. In such a limit, we can employ a time-averaging treatment for the high-frequency component $H_{\rm high}$ [1, 2], and as a result, its effective behavior is described by the following time-averaged Hamiltonian,

$$\overline{H}_{\rm high} = \hbar\left(\frac{2\Omega^2}{\delta_-'} + \frac{\Omega^2}{\delta_+'}\right)|-1\rangle\langle-1| + \hbar\left(\frac{\Omega^2}{\delta_-'} + \frac{2\Omega^2}{\delta_+'}\right)|+1\rangle\langle+1|$$
$$+ \hbar\frac{\Omega^2}{2}\left(\frac{1}{\delta_-'} + \frac{1}{\delta_+'}\right)\left\{\exp\left[i\left(\delta_- + \delta_-' - \delta_+ - \delta_+'\right)t\right]|-1\rangle\langle+1| + {\rm H.c.}\right\}, \tag{12}$$

where the first line corresponds to the energy shifts of the spin states $|\pm1\rangle$, and the second line describes a coherent coupling between these. Accordingly, the full Hamiltonian H_F is approximated to be a time-independent form,

$$H_F \simeq H_{\rm low} + \overline{H}_{\rm high}. \tag{13}$$

As seen in Sec. V, the error accumulation is strongly suppressed when $\overline{H}_{\rm high}$ is included.

Tuning $B_{\rm cnt}^{(0)} + B_z = 0$ yields $\delta_+ = \delta_- = \Delta_-$ and $\delta_+' = \delta_-' = \Delta_+$, implying that the spin states $|\pm1\rangle$ have the same Zeeman shift of $\Delta = \Delta_- + 3\Omega^2/\Delta_+$, as shown in Fig. 1(b). Therefore, we can define a bright state, $|B\rangle = (|+1\rangle + |-1\rangle)/\sqrt{2}$, which is dressed by the spin state $|0\rangle$, and a dark state, $|D\rangle = (|+1\rangle - |-1\rangle)\sqrt{2}$, which decouples from the spin state $|0\rangle$. In terms of the states $|B\rangle$ and $|D\rangle$, the full Hamiltonian becomes

$$H_F \simeq \sum_{k=1,2} \hbar\omega_k b_k^\dagger b_k + \hbar\Delta(|B\rangle\langle B| + |D\rangle\langle D|) + \hbar\sqrt{2}\Omega(|0\rangle\langle B| + |B\rangle\langle0|)$$
$$+ \sum_{k=1,2} \hbar g_k (|B\rangle\langle D| + |D\rangle\langle B|) q_k + \hbar\frac{\Omega^2}{\Delta_+}(|B\rangle\langle B| - |D\rangle\langle D|). \tag{14}$$

The dressing mechanism allows us to introduce two dressed states,

$$|\Phi_-\rangle = \cos(\theta)|0\rangle - \sin(\theta)|B\rangle, \tag{15}$$
$$|\Phi_+\rangle = \sin(\theta)|0\rangle + \cos(\theta)|B\rangle, \tag{16}$$

where $\tan(2\theta) = 2\sqrt{2}\Omega/\Delta$. Upon substituting them back into the full Hamiltonian in Eq. (14) and then using the

identity operator $\mathcal{I} = |D\rangle\langle D| + |\Phi_-\rangle\langle\Phi_-| + |\Phi_+\rangle\langle\Phi_+|$, we can straightforwardly obtain

$$
\begin{aligned}
H_F \simeq & \sum_{k=1,2} \hbar\omega_k b_k^\dagger b_k + \hbar\omega_+|\Phi_+\rangle\langle\Phi_+| + \hbar\omega_D|D\rangle\langle D| \\
& + \sum_{k=1,2} \hbar\left[g_k^{(-)}|\Phi_-\rangle\langle D| + g_k^{(+)}|D\rangle\langle\Phi_+| + \text{H.c.}\right]q_k \\
& + \hbar\frac{\Omega^2}{\Delta_+}\left[\cos(2\theta)|\Phi_+\rangle\langle\Phi_+| - \frac{1}{2}\sin(2\theta)(|\Phi_+\rangle\langle\Phi_-| + \text{H.c.}) - \cos^2(\theta)|D\rangle\langle D|\right].
\end{aligned}
\tag{17}
$$

Here,

$$
\omega_+ = \sqrt{\Delta^2 + 8\Omega^2}, \tag{18}
$$

$$
\omega_D = \frac{1}{2}\left(\Delta + \sqrt{\Delta^2 + 8\Omega^2}\right), \tag{19}
$$

$$
g_k^{(-)} = -g_k\sin(\theta), \tag{20}
$$

$$
g_k^{(+)} = g_k\cos(\theta). \tag{21}
$$

Under the assumption of $\Delta \gg \Omega$, we have $\theta \simeq 0$, such that $\sin(\theta) \simeq \sin(2\theta) \simeq 0$, $\cos(\theta) \simeq \cos^2(\theta) \simeq \cos(2\theta) \simeq 1$, $\omega_+ \simeq \Delta + 4\Omega^2/\Delta$, $\omega_D \simeq \Delta + 2\Omega^2/\Delta$, and $|\Phi_+\rangle \simeq |B\rangle$. In this limit, the coupling between $|0\rangle$ and $|B\rangle$ only causes an energy splitting, of $\simeq 2\Omega^2/\Delta$, between the states $|B\rangle$ and $|D\rangle$, so $|B\rangle$ and $|D\rangle$ can be used to define a spin qubit. Correspondingly, the full Hamiltonian is approximated as

$$
H_F' = \sum_{k=1,2} \hbar\omega_k b_k^\dagger b_k + \frac{1}{2}\hbar\omega_q\sigma_z + \sum_{k=1,2} \hbar g_k\sigma_x q_k, \tag{22}
$$

where $\omega_q = 2\Omega^2/\Delta + 2\Omega^2/\Delta_+$, $\sigma_z = |B\rangle\langle B| - |D\rangle\langle D|$, and $\sigma_x = \sigma_+ + \sigma_-$ with $\sigma_- = |D\rangle\langle B|$ and $\sigma_+ = \sigma_-^\dagger$. Modest parameters [3–9], $m_k = 1.0 \times 10^{-22}$ kg, $\omega_k/2\pi = 2$ MHz, $d_k \simeq 2$ nm, and $I_k \simeq 380$ nA, could result in a spin-CNT coupling of up to $g_k/2\pi \simeq 100$ kHz.

Furthermore, from Eq. (22) it is found that the sequential actions of the terms $\sigma_+ b_1$ and $\sigma_- b_2^\dagger$, as well as of the counter-rotating terms $\sigma_- b_1$ and $\sigma_+ b_2^\dagger$, can transfer a mechanical phonon from the left to the right CNT, and the reverse process is caused by their Hermitian conjugates. When restricting our discussion to a dispersive regime,

$$
\omega_q \pm \omega_k \gg |g_k|, \tag{23}
$$

this phonon transfer becomes dominant. Hence, in the dispersive regime the dynamics described by H_F' in Eq. (22) enables a spin quantum bus for the mechanical phonons and can be used to realize a coherent CNT-CNT coupling. In order to show more explicitly, we rewrite H_F' in the interaction picture as

$$
H_F' = \sum_{k=1,2} \hbar g_k\left\{\sigma_+ b_k\exp[i(\omega_q - \omega_k)] + \sigma_+ b_k^\dagger\exp[i(\omega_q + \omega_k)] + \text{H.c.}\right\}. \tag{24}
$$

The condition in Eq. (23) justifies to use a time-averaging treatment of the Hamiltonian H_F' [1, 2]. In the time-averaging treatment, all terms in Eq. (24) are considered as high-frequency components and exhibit time-averaged behaviors. Based on this, the dynamics of the system can be determined by an effective Hamiltonian

$$
H_{\text{eff}} = \frac{2\hbar\omega_q}{\omega_q^2 - \omega_m^2}\left[\sum_{k=1,2} g_k^2 b_k^\dagger b_k + g_1 g_2\left(b_1 b_2^\dagger + b_2 b_1^\dagger\right)\right] \otimes \sigma_z. \tag{25}
$$

Here, we have assumed that $\omega_k = \omega_m$. As expected, Eq. (25) shows a coherent spin-mediated CNT-CNT coupling, corresponding to the standard linear coupler transformation, which can give rise to a direct phonon exchange. Thus in this case, the spin qubit works as a quantum bus. At the same time, it also shows that the CNT-CNT coupling can be turned off if the intermediate spin is in the state $|0\rangle$. This is because the NV spin in the state $|0\rangle$ is decoupled from the CNTs, and the mechanical phonons can no longer be transferred from one CNT to another. Specifically, if the spin is in the state $|D\rangle$ or $|B\rangle$, the CNTs are coupled; however, if the spin is instead in the state $|0\rangle$, they are decoupled. Note that in Eq. (25) ac Stark shifts caused to be imposed on the qubit have been excluded because we focus only on the quantum states of the CNTs.

In the last part of this section, we evaluate the direct coupling between the CNTs. For simplicity, we assume that $I_k = I$, $d_k = d$, and that the CNTs have the same length L. The attractive force acting on the kth CNT is

$$\vec{F}_k = (-1)^{k-1} F \hat{y}, \tag{26}$$

where

$$F = \frac{\mu_0 L I^2}{2\pi (d - y_1 + y_2)} \tag{27}$$

is the force size. The work done by the force is given straightforwardly by

$$W = \frac{\mu_0 L I^2 (y_1 - y_2)}{2\pi (d - y_1 - y_2)}. \tag{28}$$

After applying a perturbation expansion and then a quantization, this direct CNT-CNT coupling is found to be

$$\begin{aligned} W =& \hbar W^{(1)} (b_1 - b_2 + \text{H.c.}) \\ &+ \hbar W^{(2)} \left[\left(b_1 + b_1^\dagger \right)^2 + \left(b_2 + b_2^\dagger \right)^2 - 2 \left(b_1 + b_1^\dagger \right) \left(b_2 + b_2^\dagger \right) \right], \end{aligned} \tag{29}$$

where

$$W^{(1)} = \frac{\mu_0 L I^2 y_{\text{zp}}}{2\pi d \hbar}, \tag{30}$$

$$W^{(2)} = \frac{\mu_0 L I^2 y_{\text{zp}}^2}{2\pi d^2 \hbar}. \tag{31}$$

For a modest setup [3–9], $m = 1.0 \times 10^{-22}$ kg, $\omega_m = 2\pi \times 2$ MHz, $L = 10$ nm, $d = 2$ nm, and $I = 380$ nA, we have

$$W^{(1)} \simeq 2\pi \times 20 \text{ kHz}, \tag{32}$$

which is much smaller than the mechanical resonance frequency ω_m, and also have

$$W^{(2)} \simeq 2\pi \times 1 \text{ kHz}, \tag{33}$$

which is much smaller than the spin-mediated CNT-CNT coupling, for example, $\simeq 2\pi \times 12$ kHz, as shown in the section below. Therefore, the direct CNT-CNT coupling can be neglected in our setup.

II. Controlled Hadamard gate, phase gate, and mechanical quantum delayed-choice experiment

In order to implement a quantum delayed-choice experiment with macroscopic CNT mechanical resonators, we need a controlled Hadamard gate and a phase gate to act on the CNT mechanical modes. Below, we demonstrate how the effective Hamiltonian in Eq. (25) can be used to make all required gates. Let us first consider the controlled Hadamard gate. Tuning the currents to be $I_k = I$ and, at the same time, the distances to be $d_k = d$ results in a symmetric coupling $g_k = g$. The effective Hamiltonian H_{eff} is accordingly reduced to $H_{\text{eff}} = H_{\text{cnt}} \otimes \sigma_z$, where

$$H_{\text{cnt}} = \hbar J \left(\sum_{k=1,2} b_k^\dagger b_k + b_1 b_2^\dagger + b_2 b_1^\dagger \right) \tag{34}$$

is a beam-splitter-type interaction, and where

$$J = \frac{2g^2 \omega_q}{\omega_q^2 - \omega_m^2} \tag{35}$$

is an effective CNT-CNT coupling strength. In our discussion, the NV spin is restricted to a subspace spanned by $\{|0\rangle, |D\rangle\}$, where the spin is a control qubit of a Hadamard gate. The spin in the state $|D\rangle$ mediates the coherent coupling between the separated CNTs, and causes them to evolve under the Hamiltonian H_{cnt} in Eq. (34). According

to the Heisenberg equation of motion, $b_k(t) = \exp(iH_{\text{cnt}}t/\hbar) b_k \exp(-iH_{\text{cnt}}t/\hbar)$, the unitary evolution for a time $t = \tau_0 \equiv \pi/(4J)$ corresponds to a Hadamard-like gate,

$$b_1(\tau_0) = \frac{1}{\sqrt{2}}(b_1 - ib_2), \tag{36}$$

$$b_2(\tau_0) = \frac{1}{\sqrt{2}}(b_2 - ib_1). \tag{37}$$

However, when the spin state is $|0\rangle$, the two CNTs decouple from each other. In this case, their quantum states remain unchanged under the unitary evolution, yielding

$$b_1(t) = b_1, \tag{38}$$
$$b_2(t) = b_2. \tag{39}$$

We have therefore achieved a spin-controlled Hadamard gate between the CNTs. That is, if the NV spin is in the state $|D\rangle$, then the Hadamard operation is applied to the CNTs, and if the NV spin is in the state $|0\rangle$, then the states of the CNTs are unchanged.

We next consider the phase gate. For the phase gate, we tune the currents to be $I_1 \neq 0$ and $I_2 = 0$, such that $g_1 = g$ and $g_2 = 0$, causing the effective Hamiltonian in Eq. (25) to become

$$H_{\text{cnt}} = \hbar J b_1^\dagger b_1 \sigma_z. \tag{40}$$

We find from Eq. (40) that there exists a spin-induced shift, J, of the mechanical resonance. This dispersive shift can, in turn, introduce a dynamical phase, $\phi(t) = Jt$, onto the first CNT. With the spin being in the state $|D\rangle$, we solve the Heisenberg equations of motion for the CNTs, and then obtain a phase gate,

$$b_1(t) = \exp[i\phi(t)] b_1, \tag{41}$$
$$b_2(t) = b_2. \tag{42}$$

In fact, similar to the controlled Hadamard gate discussed above, the phase gate can also be controlled by the spin according to Eq. (40).

Having achieved all required gates, we now turn to the detailed description of the macroscopic quantum delayed-choice experiment with CNT resonators. The hybrid system is initially prepared in the state $|\Psi\rangle_i \equiv |\Psi(0)\rangle = \left(b_1^\dagger \otimes \mathcal{I}_2|\text{vac}\rangle\right) \otimes |D\rangle$, where $|\text{vac}\rangle$ refers to the phonon vacuum of the CNTs and $\mathcal{I}_2$ is the identity operator on the second CNT. First, we turn on the currents of the CNTs and ensure $I_k = I$. After a time τ_0, a Hadamard operation is applied to the CNTs and accordingly, $|\Psi\rangle_i$ becomes

$$|\Psi(\tau_0)\rangle = \frac{1}{\sqrt{2}}\left(b_1^\dagger + ib_2^\dagger\right)|\text{vac}\rangle|D\rangle. \tag{43}$$

Then, we turn off the current of the second CNT for a phase accumulation for a time τ_1. As a consequence, the system further evolves to

$$|\Psi(\tau_0 + \tau_1)\rangle = \frac{1}{\sqrt{2}}\left[\exp(i\phi) b_1^\dagger + ib_2^\dagger\right]|\text{vac}\rangle|D\rangle. \tag{44}$$

While achieving the desired phase ϕ, we make a spin single-qubit rotation $|D\rangle \to \cos(\varphi)|0\rangle + \sin(\varphi)|D\rangle$, and have

$$|\Psi(\tau_0 + \tau_1)\rangle = \frac{1}{\sqrt{2}}\left[\exp(i\phi) b_1^\dagger + ib_2^\dagger\right]|\text{vac}\rangle(\cos\varphi|0\rangle + \sin\varphi|D\rangle). \tag{45}$$

Here, note that, we have ignored the length of the driving pulse of the spin rotation as being of the order of ns, and thus assumed that the state of the CNTs remains unchanged. At the end of the driving pulse, we turn on the current of the second CNT again and hold for another τ_0 to perform a Hadamard gate. This gate is in a quantum superposition of being present and absent. The three operations on the mechanical phonon correspond to the actions, on a single photon, of the input beam splitter, the phase shifter, and the output beam splitter, respectively, in quantum delayed-choice experiments with a Mach-Zehnder interferometer. The final state is therefore given by

$$|\Psi\rangle_f \equiv |\Psi(2\tau_0 + \tau_1)\rangle = \cos(\varphi)|\text{particle}\rangle|0\rangle + \sin(\varphi)|\text{wave}\rangle|D\rangle, \tag{46}$$
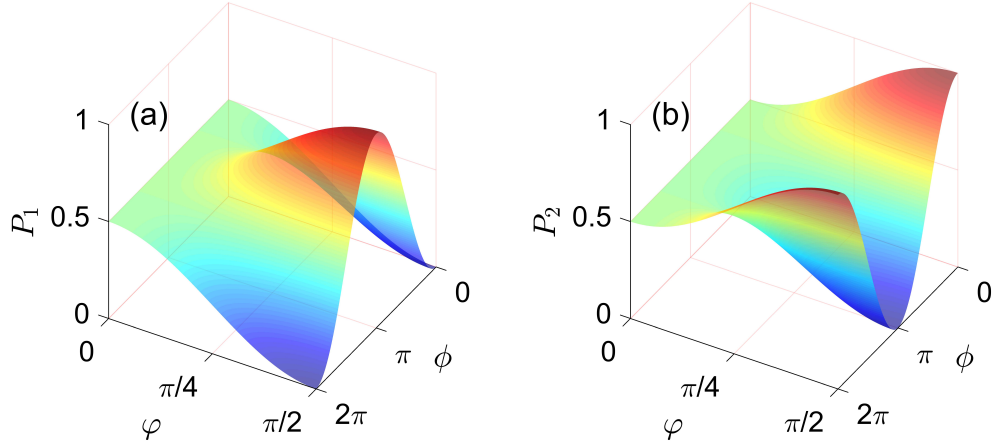
FIG. 2. (Color online) (a) Probability P_1 and (b) P_2 as a function of the rotation angle φ and the relative phase ϕ. This represents a continuous transition between a particle-type behavior ($\varphi = 0$) and a wave-type behavior ($\varphi = \pi/2$).

where

$$|\text{particle}\rangle = \frac{1}{\sqrt{2}} \left[\exp\left(i\phi\right) b_1^\dagger + i b_2^\dagger \right] |\text{vac}\rangle, \tag{47}$$

$$|\text{wave}\rangle = \frac{1}{2} \left\{ \left[\exp\left(i\phi\right) - 1\right] b_1^\dagger + i \left[\exp\left(i\phi\right) + 1\right] b_2^\dagger \right\} |\text{vac}\rangle, \tag{48}$$

describe particle and wave behaviors, respectively. This reveals that the CNT mechanical phonon is in a quantum superposition of both a particle and a wave. The probability of finding a single phonon in the kth CNT is expressed as

$$P_k = \frac{1}{2} + (-1)^k \frac{1}{2} \sin^2\left(\varphi\right) \cos\left(\phi\right), \tag{49}$$

according to Eq. (46). In Fig. 2, we have plotted the probabilities P_1 and P_2 versus the rotation angle φ and the relative phase ϕ. In this figure we find that the mechanical phonon shows a morphing behavior between particle ($\varphi = 0$) and wave ($\varphi = \pi/2$).

We now consider the timing errors of the Hadamard and phase gates. We first consider the Hadamard gate. We assume that the error of the time required for performing the Hadamard gate is δ_0, such that the actual evolution time for the gate becomes $\tau_0' = \tau_0 + \delta_0$. In order to estimate the effect of this timing error on the gate performance, we introduce a gate fidelity, defined as

$$\mathcal{F}_0 = \langle \Psi_{\text{target},0} | \rho_{\text{actual},0}\left(\tau_0'\right) | \Psi_{\text{target},0} \rangle, \tag{50}$$

where $|\Psi_{\text{target},0}\rangle$ is the target state given by the ideal Hadamard gate, and $\rho_{\text{actual},0}\left(\tau_0'\right)$ is the actual state obtained by integrating the exact master equation, given by Eq. (122). In Fig. 3, we plot the gate fidelity, F_0, versus the timing error δ_0 (red curve). In this figure, the initial state for the Hadamard gate is assumed to be $b_1^\dagger |\text{vac}\rangle |D\rangle$, so that the target state is $|\Psi_{\text{target},0}\rangle = \frac{1}{\sqrt{2}} \left(b_1^\dagger + i b_2^\dagger \right) |\text{vac}\rangle |D\rangle$. Here, $|\text{vac}\rangle$ represents the acoustic vacuum state of the CNT resonators. From this figure, we find that for $-0.32\tau_0 \lesssim \delta_0 \lesssim 0.34\tau_0$, the gate fidelity $\mathcal{F}_0$ can be kept above 0.9.

For the phase gate, we assume, as above, that the timing error is δ_1. Thus, the actual evolution time for the phase gate is $\tau_1' = \tau_1 + \delta_1$. We also introduce a gate fidelity, defined as

$$\mathcal{F}_1 = \langle \Psi_{\text{target},1} | \rho_{\text{actual},1}\left(\tau_1'\right) | \Psi_{\text{target},1} \rangle, \tag{51}$$

where $|\Psi_{\text{target},1}\rangle$ is the target state given by the ideal phase gate, and $\rho_{\text{actual},1}\left(\tau_1'\right)$ is the actual state obtained from the exact master equation, given in Eq. (122). The gate fidelity $\mathcal{F}_1$ is plotted as a function of the timing error δ_1 in Fig. (3) (blue curve). There, we assumed that the initial state for the phase gate is $\frac{1}{\sqrt{2}} \left(b_1^\dagger + i b_2^\dagger \right)$, and that the phase accumulated is equal to π. The target state $|\Psi_{\text{target},1}\rangle$ is, therefore, given by $\frac{1}{\sqrt{2}} \left(-b_1^\dagger + i b_2^\dagger \right)$. It is seen from this figure that, as long as $-0.15\tau_1 \lesssim \delta_1 \lesssim 0.12\tau_1$, we can obtain the gate fidelity of $\mathcal{F}_1 > 0.9$.
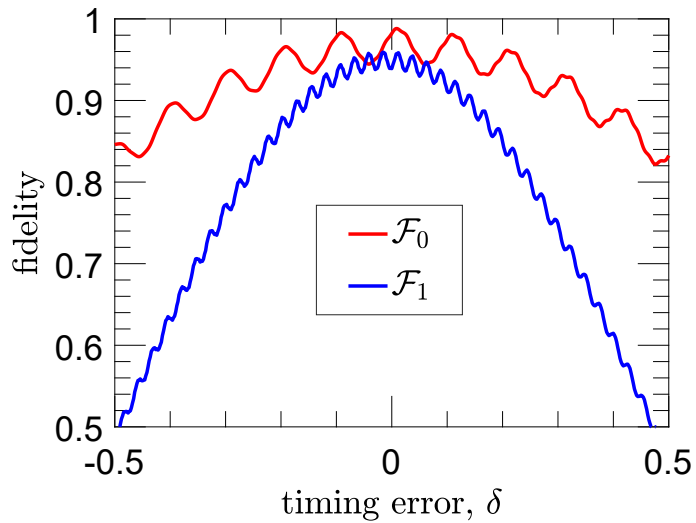
FIG. 3. (Color online) Gate fidelity as a function of the timing error. We have assumed that $\delta_0/\tau_0 = \delta_1/\tau_1 = \delta$, and that the initial state is: (i) $b_1^\dagger|\text{vac}\rangle|D\rangle$ for the Hadamard gate, and (ii) $\frac{1}{\sqrt{2}}\left(b_1^\dagger + ib_2^\dagger\right)|\text{vac}\rangle|D\rangle$ for the phase gate that accumulates a relative phase π. Here, in addition to $\gamma_s/2\pi = 200\gamma_m/2\pi = 80$ Hz, we have assumed that $g/2\pi = 100$ kHz, $\omega_m/2\pi = 2$ MHz, $\Omega = 10\omega_m$, and $\Delta_- = 142\omega_m$, resulting in $\omega_q \simeq 1.5\omega_m$ and then $J/2\pi \simeq 12$ kHz. We have also assumed that $n_{\text{th}} = 100$, which corresponds to the environment temperature of $\simeq 10$ mK.
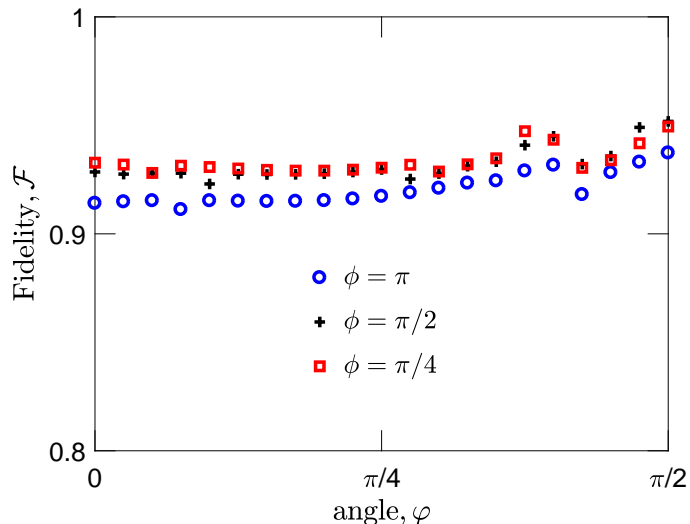

FIG. 4. (Color online) (a) Fidelity $\mathcal{F}$ as a function of the rotation angle φ. All the results are numerically obtained by integrating the exact master equation in Eq. (122). Here, in addition to $\gamma_s/2\pi = 200\gamma_m/2\pi = 80$ Hz, we have assumed that $g/2\pi = 100$ kHz, $\omega_m/2\pi = 2$ MHz, $\Omega = 10\omega_m$, and $\Delta_- = 142\omega_m$, resulting in $\omega_q \simeq 1.5\omega_m$ and then $J/2\pi \simeq 12$ kHz. We have also assumed that $n_{\text{th}} = 100$, which corresponds to an environmental temperature of $\simeq 10$ mK.

Note that the spin, in a classical mixed state of the form $\cos^2(\varphi)|0\rangle\langle0| + \sin^2(\varphi)|D\rangle\langle D|$, would lead to the same measured statistics in Eq. (49), that is, a local hidden variable model is capable of reproducing the quantum predictions. This is a loophole [10–13]. However, as discussed in Refs. [14–17], this loophole can be avoided as long as the second Hadamard operation is ensured to be in a truly quantum superposition of being present and absent. In our proposal, the second Hadamard operation is conditioned on the spin state. If the spin is in the $|0\rangle$ state, then the Hadamard operation is absent; if the spin is in the $|D\rangle$ state, then the Hadamard operation is present; if the spin is in a quantum superposition of the $|0\rangle$ and $|D\rangle$ states, then the Hadamard operation is in a quantum superposition of being present and absent. To confirm such a quantum superposition, in Fig. (4) we numerically calculate the fidelity, $\mathcal{F} = {}_f\langle\Psi|\rho_{\text{actual}}(\tau_T)|\Psi\rangle_f$, between the desired state $|\Psi\rangle_f$ in Eq. (46) and the actual state $\rho_{\text{actual}}(\tau_T)$ obtained from the exact master equation in Eq. (122). From this figure, we find that the fidelity is very close to unity even for the

finite temperature of $T \simeq 10$ mK. Furthermore, in experiments, in order to exclude the classical interpretation and prove the existence of the coherent wave-particle superposition, the quantum coherence between the states $|0\rangle$ and $|D\rangle$ should be verified. Experimentally, this coherence can be prepared by a spin single-qubit operation [18–20], and can be verified by performing quantum state tomography to show all the elements of the density matrix of the spin [20].

III. Phonon occupation at finite temperatures

We begin by considering the total operation time, which is given by $\tau_T = 2\tau_0 + \tau_1$, as discussed in Sec. II. Here, $\tau_0 = \pi/(4J)$ is the time for the Hadamard gate and $\tau_1 \in [0, 2\pi/J]$ is the time for the phase gate. In a realistic setup, we can assume $\omega_m/2\pi \simeq 2$ MHz, $\omega_q/2\pi \simeq 3$ MHz, and $g/2\pi = 100$ kHz, such that $J/2\pi \simeq 12$ kHz, yielding a maximum total time $\tau_T^{\max} = 2\tau_0 + \tau_1^{\max} \simeq 0.1$ ms, where $\tau_1^{\max} = 2\pi/J$ is the maximum phase gate time. Note that, the operation time τ_T depends inversely on the CNT-CNT coupling strength J, but the enhancement in J is limited by the validity of the effective Hamiltonian H_{eff}.

The total decoherence in our setup can be divided into two parts, one from the spin and the other from the CNTs. The spin decoherence in general includes the relaxation and the dephasing. For an NV electronic spin, the relaxation time T_1 can reach up to several minutes at low temperatures and the dephasing time can be $T_2 \simeq 2$ ms even at room temperature [21, 22]. These justify neglecting the spin decoherence. For the mechanical decoherence, despite a long phonon life, the low mechanical frequency makes the CNT mechanical modes very sensitive to the environmental temperature. In this section and in Sec. IV, we discuss the effects of the mechanical noise on our quantum delayed-choice experiment, and demonstrate that the morphing between wave and particle can still be effectively observed even at finite temperatures.

As a result, the dissipative processes, in the hybrid system considered here, are induced only by the mechanical decoherence, which arises from the vacuum fluctuation and thermal noise. The full dynamics of the system can then be governed by the following master equation

$$\dot{\rho}(t) = \frac{i}{\hbar} [\rho(t), H(t)] - \frac{\gamma_m}{2} n_{\text{th}} \sum_{k=1,2} \mathcal{L}\left(b_k^\dagger\right) \rho(t) - \frac{\gamma_m}{2} (n_{\text{th}} + 1) \sum_{k=1,2} \mathcal{L}(b_k) \rho(t), \tag{52}$$

where ρ is the density operator of the system, γ_m is the mechanical decay rate, $n_{\text{th}} = [\exp(\hbar\omega_m/k_B T) - 1]^{-1}$ is the equilibrium phonon occupation at temperature T, and $\mathcal{L}(o)\rho(t) = o^\dagger o \rho(t) - 2o\rho(t) o^\dagger + \rho(t) o^\dagger o$ is the Lindblad superoperator. Here, $H(t)$ is a binary Hamiltonian of the form,

$$H(t) = \begin{cases} H_0, & 0 < t \leq \tau_0, \text{ and } \tau_0 + \tau_1 < t \leq \tau_T \\ H_1, & \tau_0 < t \leq \tau_0 + \tau_1, \end{cases} \tag{53}$$

with

$$H_0 = \hbar J \left(\sum_{k=1,2} b_k^\dagger b_k + b_1 b_2^\dagger + b_2 b_1^\dagger \right) \sigma_z, \tag{54}$$

$$H_1 = \hbar J b_1^\dagger b_1 \sigma_z. \tag{55}$$

The three time intervals in Eq. (53) correspond to the first Hadamard gate, the phase gate and the second Hadamard gate, respectively. Note that in Eq. (53), we did not include the spin single-qubit rotation before the third interval because the length of the driving pulse is of the order of ns. We can derive the system evolution step by step.

Let us now consider the first evolution interval $0 < t \leq \tau_0$. During this interval, the coupling of the CNT mechanical modes introduces two delocalized phononic modes,

$$c_\pm = \frac{1}{\sqrt{2}} (b_1 \pm b_2), \tag{56}$$

such that H_0 is diagonalized to be

$$H_0 = 2\hbar J c_+^\dagger c_+ \sigma_z, \tag{57}$$

and the master equation in Eq. (52) is reexpressed, in terms of the modes $c_\pm$, as

$$\dot{\rho} = i \left[\rho, 2J c_+^\dagger c_+ \sigma_z \right] - \frac{\gamma_m}{2} n_{\text{th}} \sum_{\mu=1,2} \mathcal{L}\left(c_\mu^\dagger\right) \rho(t) - \frac{\gamma_m}{2} (n_{\text{th}} + 1) \sum_{\mu=1,2} L(c_\mu) \rho(t). \tag{58}$$

In order to calculate the phonon occupations at the end of the first interval, we need to obtain the equations of motion for $\langle c_\pm^\dagger c_\pm \rangle$, $\langle c_+^\dagger c_- \rangle$, $\langle c_+^\dagger c_- \sigma_z \rangle$, and $\langle c_+^\dagger c_- \sigma_z^2 \rangle$. Here, $\langle O \rangle$ represents the expectation value of the operator O. Following the master equation in Eq. (58), we have

$$\frac{d}{dt}\langle c_\pm^\dagger c_\pm \rangle = - \gamma_m \langle c_\pm^\dagger c_\pm \rangle + \gamma_m n_{\text{th}}, \tag{59}$$

$$\frac{d}{dt}\langle c_+^\dagger c_- \rangle = i2J\langle c_+^\dagger c_- \sigma_z \rangle - \gamma_m \langle c_+^\dagger c_- \rangle, \tag{60}$$

$$\frac{d}{dt}\langle c_+^\dagger c_- \sigma_z \rangle = i2J\langle c_+^\dagger c_- \sigma_z^2 \rangle - \gamma_m \langle c_+^\dagger c_- \sigma_z \rangle, \tag{61}$$

$$\frac{d}{dt}\langle c_+^\dagger c_- \sigma_z^2 \rangle = i2J\langle c_+^\dagger c_- \sigma_z \rangle - \gamma_m \langle c_+^\dagger c_- \sigma_z^2 \rangle, \tag{62}$$

where we have used the relation $\sigma_z^3 = \sigma_z$. We can straightforwardly solve the differential equation (59) to find

$$\langle c_\pm^\dagger c_\pm \rangle (t) = \left(\frac{1}{2} - n_{\text{th}}\right) \exp\left(-\gamma_m t\right) + n_{\text{th}}. \tag{63}$$

Combining Eqs. (61) and (62) gives

$$\langle c_+^\dagger c_- \sigma_z^j \rangle (t) = (-1)^j \frac{1}{2} \exp\left(-i2Jt\right) \exp\left(-\gamma_m t\right), \tag{64}$$

for $j = 1, 2$. Upon substituting Eq. (64) back into Eq. (60), we can then obtain

$$\langle c_+^\dagger c_- \rangle (t) = \frac{1}{2} \exp\left(-i2Jt\right) \exp\left(-\gamma_m t\right). \tag{65}$$

It is found, according to Eq. (56), that in the localized-mode basis,

$$\langle b_k^\dagger b_k \rangle (\tau_0) = \left(\frac{1}{2} - n_{\text{th}}\right) \exp\left(-\gamma_m \tau_0\right) + n_{\text{th}}, \tag{66}$$

$$\langle b_1^\dagger b_2 \rangle (\tau_0) = \frac{i}{2} \exp\left(-\gamma_m \tau_0\right). \tag{67}$$

For the second evolution interval $\tau_0 < t \leq \tau_0 + \tau_1$, we directly use the master equation in Eq. (52) but with $H(t)$ replaced by H_1. When comparing with the master equation in Eq. (58), we see that the equations of motion for $\langle b_k^\dagger b_k \rangle$, $\langle b_1^\dagger b_2 \rangle$, $\langle b_1^\dagger b_2 \sigma_z \rangle$, and $\langle b_1^\dagger b_2 \sigma_z^2 \rangle$ should have the same forms as in Eqs. (59), (60), (61), and (62), but with the substitutions $c_+ \to b_1$, $c_- \to b_2$ and $2J \to J$. In combination with the initial conditions, given in Eqs. (66) and (67), we follow the same procedure as above to find

$$\langle b_k^\dagger b_k \rangle (\tau_0 + \tau_1) = \left(\frac{1}{2} - n_{\text{th}}\right) \exp\left[-\gamma_m (\tau_0 + \tau_1)\right] + n_{\text{th}}, \tag{68}$$

$$\langle b_1^\dagger b_2 \rangle (\tau_0 + \tau_1) = \frac{i}{2} \exp\left(-iJ\tau_1\right) \exp\left[-\gamma_m (\tau_0 + \tau_1)\right]. \tag{69}$$

We now turn to the third evolution interval $\tau_0 + \tau_1 < t \leq 2\tau_0 + \tau_1$. Before this interval or at the end of the second interval, we apply a single qubit rotation, $|D\rangle \to \cos(\varphi)|0\rangle + \sin(\varphi)|D\rangle$, on the NV spin to engineer the subsequent Hadamard operation to be in a quantum superposition of being absent and present. In this situation, we still use the delocalized-mode basis and the corresponding master equation in Eq. (58). According to Eqs. (68) and (69), the initial conditions of the last evolution can be rewritten, in terms of $c_\pm$, as

$$\langle c_\pm^\dagger c_\pm \rangle (\tau_0 + \tau_1) = \left[\frac{1}{2} \pm \frac{1}{2} \sin(J\tau_1) - n_{\text{th}}\right] \exp\left[-\gamma (\tau_0 + \tau_1)\right] + n_{\text{th}}, \tag{70}$$

$$\langle c_+^\dagger c_- \rangle (\tau_0 + \tau_1) = - \frac{i}{2} \cos(J\tau_1) \exp\left[-\gamma (\tau_0 + \tau_1)\right], \tag{71}$$

$$\langle c_+^\dagger c_- \sigma_z^j \rangle (\tau_0 + \tau_1) = (-1)^j \sin^2(\varphi) \langle c_+^\dagger c_- \rangle (\tau_0 + \tau_1), \tag{72}$$

for $j = 1, 2$. Then, as before, solving the differential equations in Eqs. (59), (60), (61) and (62) leads to

$$\langle c_\pm^\dagger c_\pm \rangle (t) = \left[\frac{1}{2} \pm \frac{1}{2} \sin (J\tau_1) - n_{\text{th}} \right] \exp (-\gamma_m t) + n_{\text{th}}, \tag{73}$$

$$\langle c_+^\dagger c_- \rangle (t) = -\frac{i}{2} \cos (J\tau_1) \left\{ \cos^2 (\varphi) + \sin^2 (\varphi) \exp [-i2J (t - \tau_0 - \tau_1)] \right\} \exp (-\gamma_m t), \tag{74}$$

which, in turn, gives

$$n_k \equiv \langle b_k^\dagger b_k \rangle (\tau_T) = (P_k - n_{\text{th}}) \exp (-\gamma_m \tau_T) + n_{\text{th}}, \tag{75}$$

which is the phonon occupation of the kth at the end of the third interval. For a realistic CNT, the mechanical linewidth can be set to $\gamma_m/2\pi = 0.4$ Hz [23], and then we obtain a phonon lifetime of $\simeq 400$ ms, which is much longer than the maximum total time $\tau_T^{\text{max}} \simeq 0.1$ ms. This ensures $\gamma_m \tau_T \ll 1$, which results in

$$n_k \simeq P_k + n_{\text{th}} \gamma_m \tau_T. \tag{76}$$

This shows that the occupation for each CNT has two contributions: one from a coherent phonon signal and one from thermal excitations. Furthermore, we find from Eq. (76) that the thermal excitations have equal contributions to n_1 and n_2. This is because the thermal excitations do not contribute to the interference. For an environmental temperature $T = 10$ mK, the equilibrium phonon occupation is $n_{\text{th}} \simeq 100$, yielding $n_{\text{th}} \gamma_m \tau_T^{\text{max}} \simeq 0.03$, which can be neglected, as shown in Fig. 2 of the article.

IV.   Signal-to-noise ratio at finite temperatures

In addition to the thermal occupation, $n_{\text{th}} \gamma_m \tau_T$, in Eq. (76), the desired signal P_k is also always accompanied by fluctuation noise. Such a noise includes vacuum fluctuations and thermal fluctuations. In particular, the latter increases with temperature, so that the signal can be completely drowned in the noise when the temperature is sufficiently high. In this case, it is very difficult to observe the morphing between wave and particle. Thus in this section, we analyze this fluctuation noise in detail, and demonstrate that, in order for the morphing behavior to be observed effectively, the total fluctuation noise of both CNTs should be limited by an upper bound, which leads to a critical temperature T_c.

Specifically, we begin by deriving the fluctuation δn_k in the occupation n_k, for $k = 1, 2$. This is defined by

$$(\delta n_k)^2 = \langle \left(b_k^\dagger b_k \right)^2 \rangle (\tau_T) - \langle b_k^\dagger b_k \rangle^2 (\tau_T)$$
$$= \langle b_k^\dagger b_k^\dagger b_k b_k \rangle (\tau_T) + n_k - n_k^2. \tag{77}$$

In order to understand the fluctuation noise better, we need to derive an analytical expression of δn_k. In Sec. III, n_k has been given in Eq. (76). Below, we derive the evolution of $\langle b_k^\dagger b_k^\dagger b_k b_k \rangle$ in a step-by-step manner as in Sec. III.

We now consider the first evolution interval $0 < t \leq \tau_0$. During this interval, the delocalized modes $c_\pm$ in Eq. (56) are employed owing to the coupling of the CNT mechanical modes, and the dynamics is described by the master equation in Eq. (58). To achieve $\langle b_k^\dagger b_k^\dagger b_k b_k \rangle$ at time τ_T, the dynamical evolutions of $\langle c_\pm^\dagger c_\pm^\dagger c_\pm c_\pm \rangle$, $\langle c_+^\dagger c_+ c_-^\dagger c_- \rangle$, $\langle c_+^\dagger c_+^\dagger c_+ c_- \rangle$, $\langle c_+^\dagger c_-^\dagger c_- c_- \rangle$, and $\langle c_+^\dagger c_+^\dagger c_- c_- \rangle$ are involved. The equations of motion for $\langle c_\pm^\dagger c_\pm^\dagger c_\pm c_\pm \rangle$ and $\langle c_+^\dagger c_+ c_-^\dagger c_- \rangle$ are

$$\frac{d}{dt} \langle c_\pm^\dagger c_\pm^\dagger c_\pm c_\pm \rangle = 4\gamma_m n_{\text{th}} \langle c_\pm^\dagger c_\pm \rangle - 2\gamma_m \langle c_\pm^\dagger c_\pm^\dagger c_\pm c_\pm \rangle, \tag{78}$$

$$\frac{d}{dt} \langle c_+^\dagger c_+ c_-^\dagger c_- \rangle = \gamma_m n_{\text{th}} \left(\langle c_+^\dagger c_+ \rangle + \langle c_-^\dagger c_- \rangle \right) - 2\gamma_m \langle c_+^\dagger c_+ c_-^\dagger c_- \rangle. \tag{79}$$

Substituting Eq. (63) yields

$$\langle c_\pm^\dagger c_\pm^\dagger c_\pm c_\pm \rangle (\tau_0) = 2X (\tau_0), \tag{80}$$

$$\langle c_+^\dagger c_+ c_-^\dagger c_- \rangle (\tau_0) = X (\tau_0), \tag{81}$$

where

$$X (t) = n_{\text{th}} (n_{\text{th}} - 1) \exp (-2\gamma_m t) + n_{\text{th}} (1 - 2n_{\text{th}}) \exp (-\gamma_m t) + n_{\text{th}}^2. \tag{82}$$

The equations of motion for $\langle c_+^\dagger c_+^\dagger c_+ c_- \rangle$ are found to be

$$\frac{d}{dt}\langle c_+^\dagger c_+^\dagger c_+ c_- \rangle = i2J\langle c_+^\dagger c_+^\dagger c_+ c_- \sigma_z \rangle + 2\gamma_m n_{\text{th}}\langle c_+^\dagger c_- \rangle - 2\gamma_m \langle c_+^\dagger c_+^\dagger c_+ c_- \rangle, \tag{83}$$

$$\frac{d}{dt}\langle c_+^\dagger c_+^\dagger c_+ c_- \sigma_z \rangle = i2J\langle c_+^\dagger c_+^\dagger c_+ c_- \sigma_z^2 \rangle + 2\gamma_m n_{\text{th}}\langle c_+^\dagger c_- \sigma_z \rangle - 2\gamma_m \langle c_+^\dagger c_+^\dagger c_+ c_- \sigma_z \rangle, \tag{84}$$

$$\frac{d}{dt}\langle c_+^\dagger c_+^\dagger c_+ c_- \sigma_z^2 \rangle = i2J\langle c_+^\dagger c_+^\dagger c_+ c_- \rangle + 2\gamma_m n_{\text{th}}\langle c_+^\dagger c_- \sigma_z^2 \rangle - 2\gamma_m \langle c_+^\dagger c_+^\dagger c_+ c_- \sigma_z^2 \rangle. \tag{85}$$

Together with Eq. (64), solving straightforwardly the coupled differential equations (84) and (85) results in

$$\langle c_+^\dagger c_+^\dagger c_+ c_- \sigma_z \rangle(t) = -n_{\text{th}}\left[1 - \exp\left(-\gamma_m t\right)\right]\exp\left(-i2Jt\right)\exp\left(-\gamma_m t\right), \tag{86}$$

which, in turn, gives

$$\langle c_+^\dagger c_+^\dagger c_+ c_- \rangle(\tau_0) = -iY(\tau_0), \tag{87}$$

where

$$Y(t) = n_{\text{th}}\left[1 - \exp\left(-\gamma_m t\right)\right]\exp\left(-\gamma_m t\right). \tag{88}$$

In a treatment similar to that used for $\langle c_+^\dagger c_+^\dagger c_+ c_- \rangle$, we obtain

$$\langle c_+^\dagger c_-^\dagger c_- c_- \rangle(\tau_0) = -iY(\tau_0), \tag{89}$$

$$\langle c_+^\dagger c_+^\dagger c_- c_- \rangle(\tau_0) = 0. \tag{90}$$

Upon combining Eqs. (80), (81), (87), (89), and (90), this yields, after inversion back to the localized-mode basis,

$$\langle b_k^\dagger b_k^\dagger b_k b_k \rangle(\tau_0) = 2X(\tau_0), \tag{91}$$

$$\langle b_1^\dagger b_1 b_2^\dagger b_2 \rangle(\tau_0) = X(\tau_0), \tag{92}$$

$$\langle b_1^\dagger b_1^\dagger b_1 b_2 \rangle(\tau_0) = \langle b_1^\dagger b_2^\dagger b_2 b_2 \rangle(\tau_0) = iY(\tau_0), \tag{93}$$

$$\langle b_1^\dagger b_1^\dagger b_2 b_2 \rangle(\tau_0) = 0. \tag{94}$$

During the second evolution interval $\tau_0 < t \leq \tau_0 + \tau_1$, the dynamics of the system is driven by the master equation given in Eq. (52), but with $H(t)$ replaced by H_1. Thus, as mentioned in Sec. III, the system has a dynamical evolution similar to what has already been discussed with the delocalized-mode basis in the first interval. We follow the same recipe as above and then find

$$\langle b_k^\dagger b_k^\dagger b_k b_k \rangle(\tau_0 + \tau_1) = 2X(\tau_0 + \tau_1), \tag{95}$$

$$\langle b_1^\dagger b_1 b_2^\dagger b_2 \rangle(\tau_0 + \tau_1) = X(\tau_0 + \tau_1), \tag{96}$$

$$\langle b_1^\dagger b_1^\dagger b_1 b_2 \rangle(\tau_0 + \tau_1) = \langle b_1^\dagger b_2^\dagger b_2 b_2 \rangle(\tau_0 + \tau_1) = i\exp\left(-iJ\tau_1\right)Y(\tau_0 + \tau_1), \tag{97}$$

$$\langle b_1^\dagger b_1^\dagger b_2 b_2 \rangle(\tau_0 + \tau_1) = 0, \tag{98}$$

at the end of this interval.

For the third evolution interval $\tau_0 + \tau_1 < t \leq \tau_T$, we return back to the master equation in Eq. (58), and also back to the delocalized-mode basis. According to Eqs. (95), (96), (97), and (98), the evolution at this stage starts from

$$\langle c_\pm^\dagger c_\pm^\dagger c_\pm c_\pm \rangle(\tau_0 + \tau_1) = 2X(\tau_0 + \tau_1) \mp i2\sin\left(J\tau_1\right)Y(\tau_0 + \tau_1), \tag{99}$$

$$\langle c_+^\dagger c_+ c_-^\dagger c_- \rangle(\tau_0 + \tau_1) = X(\tau_0 + \tau_1), \tag{100}$$

$$\langle c_+^\dagger c_+^\dagger c_+ c_- \rangle(\tau_0 + \tau_1) = \langle c_+^\dagger c_-^\dagger c_- c_- \rangle(\tau_0 + \tau_1) = -i\cos\left(J\tau_1\right)Y(\tau_0 + \tau_1), \tag{101}$$

$$\langle c_+^\dagger c_+^\dagger c_+ c_- \sigma_z^j \rangle(\tau_0 + \tau_1) = \langle c_+^\dagger c_-^\dagger c_- c_- \sigma_z^j \rangle(\tau_0 + \tau_1) = i(-1)^{j+1}\sin^2\left(\varphi\right)\cos\left(J\tau_1\right)Y(\tau_0 + \tau_1), \tag{102}$$

$$\langle c_+^\dagger c_+^\dagger c_- c_- \rangle(\tau_0 + \tau_1) = \langle c_+^\dagger c_+^\dagger c_- c_- \sigma_z^j \rangle(\tau_0 + \tau_1) = 0, \tag{103}$$

where $j = 1, 2$. Note that, before this evolution, the spin state has already been transformed from $|D\rangle \to \cos(\varphi)|0\rangle + \sin(\varphi)|D\rangle$ via a single-qubit rotation. Then, by following the same procedure as in the first interval, the last evolution ends with

$$\langle c_\pm^\dagger c_\pm^\dagger c_\pm c_\pm \rangle (\tau_T) = 2X(\tau_T) \pm 2\sin(J\tau_1) Y(\tau_T), \tag{104}$$

$$\langle c_+^\dagger c_+ c_-^\dagger c_- \rangle (\tau_T) = X(\tau_T), \tag{105}$$

$$\langle c_+^\dagger c_+^\dagger c_+ c_- \rangle (\tau_T) = \langle c_+^\dagger c_-^\dagger c_- c_- \rangle (\tau_T) = -i\cos(J\tau_1) \left[\cos^2(\varphi) - i\sin^2(\varphi)\right] Y(\tau_T), \tag{106}$$

$$\langle c_+^\dagger c_+^\dagger c_- c_- \rangle (\tau_T) = 0, \tag{107}$$

and as a result, with

$$\langle b_k^\dagger b_k^\dagger b_k b_k \rangle (\tau_T) = 2X(\tau_T) + 2(-1)^j \sin^2(\varphi) \cos(J\tau_1) Y(\tau_T). \tag{108}$$

It is seen that on the right-hand side of Eq. (108), the first term arises from the particle behavior of a phonon and the second term arises from its wave behavior.

By substituting Eq. (108) into Eq. (77), the fluctuation δn_k in the occupation n_k is given by

$$\begin{aligned}(\delta n_k)^2 = & \left(n_{\mathrm{th}}^2 - 2P_k n_{\mathrm{th}} - P_k^2\right) \exp(-2\gamma_m \tau_T) \\ & - (2n_{\mathrm{th}} + 1)(n_{\mathrm{th}} - P_k) \exp(-\gamma_m \tau_T) + n_{\mathrm{th}}(n_{\mathrm{th}} + 1).\end{aligned} \tag{109}$$

Since $\gamma_m \tau_T \ll 1$, we have

$$(\delta n_k)^2 \simeq \left(\delta n_k^{\mathrm{signal}}\right)^2 + \left(\delta n_k^{\mathrm{noise}}\right)^2, \tag{110}$$

where

$$\left(\delta n_k^{\mathrm{signal}}\right)^2 = P_k(1 - P_k), \tag{111}$$

$$\left(\delta n_k^{\mathrm{noise}}\right)^2 = P_k(2P_k - 1)\gamma_m \tau_T + n_{\mathrm{th}}\gamma_m \tau_T (2P_k + 1). \tag{112}$$

Here, $\delta n_k^{\mathrm{signal}}$, the quantum fluctuation induced by the Heisenberg uncertainty principle, accounts for the coherent signal, and $\delta n_k^{\mathrm{noise}}$ represents the fluctuation noise, including the vacuum (the first term) and thermal (the second term) fluctuations. To confirm the predictions of Eq. (110), we perform numerics, as shown in Fig. 5. Specifically, we plot the fluctuation noises $\delta n_1^{\mathrm{noise}}$ and $\delta n_2^{\mathrm{noise}}$ versus the relative phase ϕ. The analytical expression is in excellent agreement with our numerical simulations. Furthermore, the respective CNT signal-to-noise ratios can be defined as
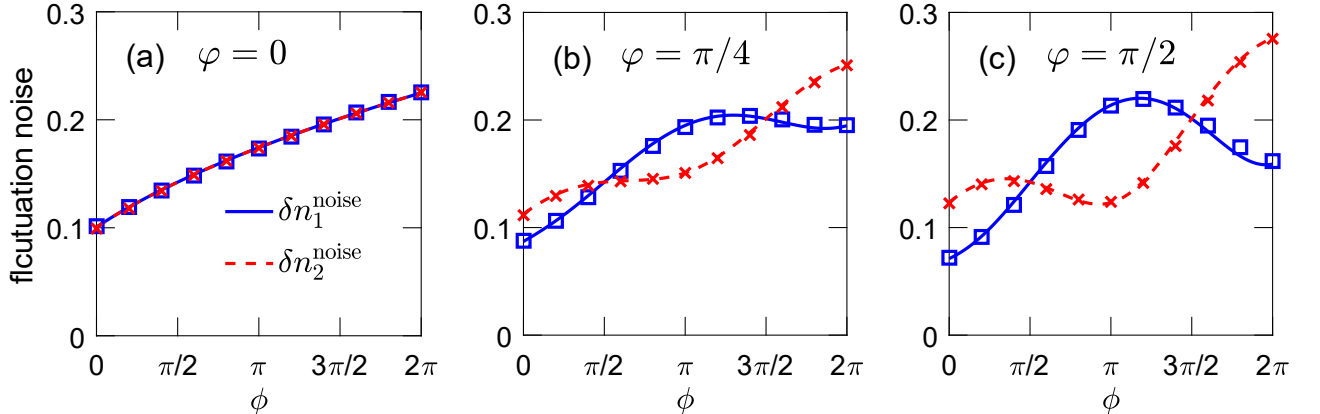

FIG. 5. (Color online) Fluctuation noise $\delta n_1^{\mathrm{noise}}$ and $\delta n_2^{\mathrm{noise}}$ as a function of the phase ϕ. (a) $\varphi = 0$, (b) $\pi/4$, and (c) $\pi/2$. Solid and dashed curves are analytical results for $\delta n_1^{\mathrm{noise}}$ and $\delta n_2^{\mathrm{noise}}$, respectively, and symbols correspond to numerical simulations. These analytical and numerical results exhibit an exact agreement. For all plots, in addition to $\gamma_s/2\pi = 200\gamma_m/2\pi = 80$ Hz, we have assumed that $g/2\pi = 100$ kHz, $\omega_m/2\pi = 2$ MHz, $\Omega = 10\omega_m$, and $\Delta_- = 142\omega_m$, resulting in $\omega_q \simeq 1.5\omega_m$ and then $J/2\pi \simeq 12$ kHz. We have also assumed that $n_{\mathrm{th}} = 100$, corresponding to an environmental temperature of $\simeq 10$ mK.
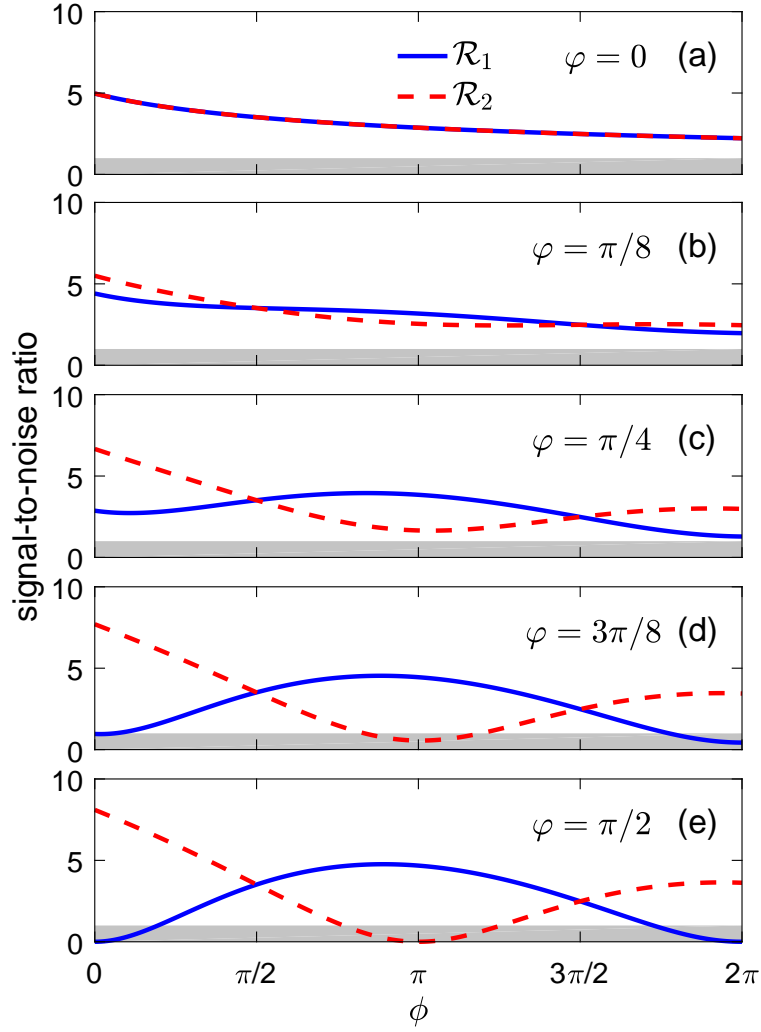
FIG. 6. (Color online) Signal-to-noise ratios $\mathcal{R}_1$ and $\mathcal{R}_2$. (a) $\varphi = 0$, (b) $\pi/8$, (c) $\pi/4$, (d) $3\pi/8$, and (e) $\pi/2$. The solid curves show $\mathcal{R}_1$, while the dashed curves show $\mathcal{R}_2$. The gray shaded area represents the region, where the signal cannot be resolved. For all plots, all other parameters have been set to be the same as in Fig. 5.

$$\mathcal{R}_k = \frac{P_k}{\delta n_k^{\mathrm{noise}}}. \tag{113}$$

Note that, here, we did not use δn_k to define $\mathcal{R}_k$ because $\delta n_k^{\mathrm{signal}}$ in δn_k results from quantum fluctuations of the desired signal, as mentioned previously; and therefore this is not the environmental noise. In order to resolve a signal from the fluctuation noise, the ratio $\mathcal{R}_k$ is required to be $\mathcal{R}_k > 1$. However, Eq. (113) demonstrates that this criterion is not always met for all values of P_k, in particular, at finite temperatures. For example, $P_k = 0$ leads directly to $\mathcal{R}_k = 0$. To address this problem, we now consider the total fluctuation noise,

$$\mathcal{S}^2 = \left(\delta n_1^{\mathrm{noise}}\right)^2 + \left(\delta n_2^{\mathrm{noise}}\right)^2. \tag{114}$$

We further assume that

$$\mathcal{S}^2 < P_1^2 + P_2^2. \tag{115}$$

Under this assumption, if $\mathcal{R}_k < 1$, then $\mathcal{R}_{3-k} > 1$ for $k = 1, 2$; otherwise $\mathcal{R}_1 > 1$, $\mathcal{R}_2 > 1$. This means that at least one of the signals, P_1 or P_2, is resolved for each measurement. Because the coherent phonon number equal to 1 is conserved, and therefore the signals in the two CNTs are complementary, the unresolved signal can be completely deduced from the resolved one. Thus, the criterion in Eq. (115) ensures that the morphing behavior between wave

and particle can be observed from the environment-induced fluctuation noise. In fact, for any value of P_k, the total noise $\mathcal{S}$ is limited by an upper bound,

$$\mathcal{S} < \mathcal{B} \equiv \sqrt{\gamma_m \tau_T^{\max} + 4 n_{\text{th}} \gamma_m \tau_T^{\max}}, \tag{116}$$

which is independent of P_k. Meanwhile, $\sqrt{P_1^2 + P_2^2}$ is also limited by a lower bound $\sqrt{2}/2$. Thereby, in order to meet the criterion given in Eq. (115), it is required that

$$\mathcal{B} < \frac{\sqrt{2}}{2}. \tag{117}$$

Based on this condition, we can define a signal visibility

$$\mathcal{R} = \frac{\sqrt{2}}{2\mathcal{B}}, \tag{118}$$

in analogy to R_k. When $\mathcal{R} > 1$, the morphing between wave and particle can be observed, and cannot otherwise. This, in turn, leads to an upper bound on the equilibrium phonon occupation,

$$n_{\text{th}} < \frac{1 - 2\gamma_m \tau_T^{\max}}{8\gamma_m \tau_T^{\max}}, \tag{119}$$

and therefore an upper bound on the temperature,

$$T < \frac{\hbar \omega_m}{k_B \ln\left[\left(1 + 6\gamma_m \tau_T^{\max}\right) / \left(1 - 2\gamma_m \tau_T^{\max}\right)\right]}. \tag{120}$$

Because $\tau_T^{\max} \simeq 5\pi/2J$, the critical temperature is

$$T_{\text{c}} = \frac{\hbar \omega_m}{k_B \ln\left[\left(1 + 15\pi\gamma_m/J\right) / \left(1 - 5\pi\gamma_m/J\right)\right]}. \tag{121}$$

In Fig. 6 we plot the signal-to-noise ratios $\mathcal{R}_1$ and $\mathcal{R}_2$ at the temperature $T \simeq 10$ mK. We find that almost all signals can be resolved, and also, as expected, find that when the signal in one CNT is unresolved, the signal in the other CNT is resolved. In fact, the upper bound $\mathcal{B}$ is the fluctuation noise in the total phonon occupation $\langle b_1^\dagger b_1 + b_2^\dagger b_2 \rangle$ at time τ_T. The criterion $\mathcal{R} > 1$ heralds that to resolve the morphing behavior, the fluctuation noise in $\langle b_1^\dagger b_1 + b_2^\dagger b_2 \rangle (\tau_T)$ is required to be smaller than $\sqrt{2}/2$.

V. Numerical simulations

In order to confirm our analytical results, we need to numerically simulate the dynamics with the full master equation given by

$$
\begin{aligned}
\dot{\rho}(t) =& \frac{i}{\hbar}\left[\rho(t), H_F\right] - \frac{\gamma_s}{2}\mathcal{L}(\sigma_z')\rho(t) \\
& - \frac{\gamma_m}{2} n_{\text{th}} \sum_{k=1,2} \mathcal{L}\left(b_k^\dagger\right)\rho(t) - \frac{\gamma_m}{2}\left(n_{\text{th}} + 1\right)\sum_{k=1,2} \mathcal{L}(b_k)\rho(t),
\end{aligned}
\tag{122}
$$

where $\sigma_z' = |D\rangle\langle D| - |0\rangle\langle 0|$, and H_F is the full Hamiltonian of Eq. (8). Here, we use the Python framework QuTiP [24, 25] to set up this problem. However, the full Hamiltonian is time-dependent, and it takes a long time to integrate the corresponding Schrödinger equation or the master equation, in particular, for our case, where all quantum gates result from the deterministic time evolution of the system. Thus, in our numerical simulations, we replace H_F with $H_{\text{low}} + \overline{H}_{\text{high}}$, as in Eq. (13). This is a reasonable replacement because in our proposal Ω (tens of MHz) is required to be much smaller than Δ' (up to $\sim$ GHz). In Fig. 7, we plot the unitary evolution of the phonon occupations, $\langle b_1^\dagger b_1 \rangle$ and $\langle b_2^\dagger b_2 \rangle$, of the CNTs. Symbols are the exact results from the full Hamiltonian H_F and solid curves are given by the approximate Hamiltonian $H_{\text{low}} + \overline{H}_{\text{high}}$. We find an excellent agreement for a very long evolution time, and thus H_F can be very well approximated by $H_{\text{low}} + \overline{H}_{\text{high}}$. For additional comparison, we also plot the phonon occupation evolution driven only by the low-frequency component H_{low}, corresponding to dotted curves. As seen in Fig. 7, owing to the error accumulation, the dynamics of H_{low} deviates largely from the full dynamics of H_F, even within one oscillation cycle. With the above replacement, we obtain the numerical simulations plotted in Fig. 2 of the article, and also in Fig. 5 of the Supplemental Material.
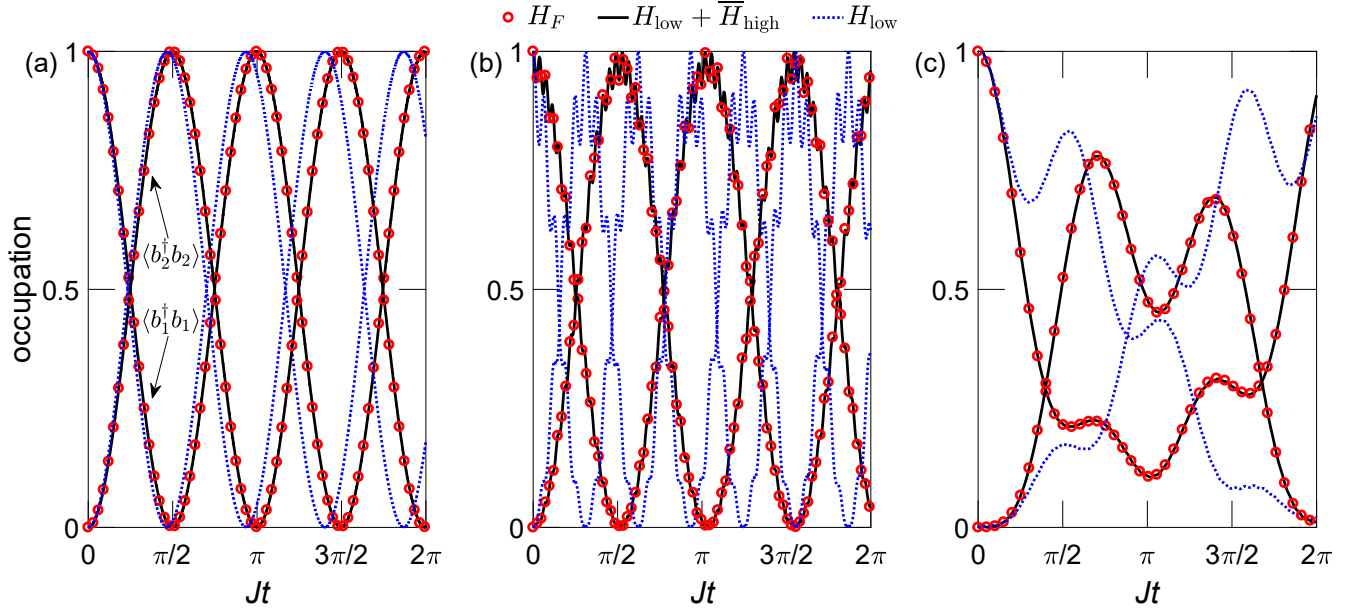
FIG. 7. (Color online) Unitary evolution of the CNT phonon occupations, $\langle b_1^\dagger b_1 \rangle$ and $\langle b_2^\dagger b_2 \rangle$, for (a) $\Delta_- = 10\Omega$, (b) 25Ω, and (c) 35Ω. The symbols, solid, and dotted curves are obtained, respectively, from H_F, $H_{low} + H_{high}$, and H_{low}. For all plots here we have assumed that $\omega_m/2\pi = 2$ MHz, $\Omega = 15\omega_m$, $\omega_0 = D - \Delta_-$, $\Delta_+ = D + \omega_0$, $\Delta = \Delta_- + 3\Omega^2/\Delta_+$, $\omega_q = 2\Omega^2/\Delta + 2\Omega^2/\Delta_+$, and $J = 2\omega_q g^2/\left(\omega_q^2 - \omega_m^2\right)$, with a symmetric coupling strength $g/2\pi = 100$ kHz and an initial state $|\Psi\rangle_i = \left(b_1^\dagger \otimes \mathcal{I}_2 |\text{vac}\rangle\right) \otimes |D\rangle$.

[1] Gamel, O. & James, D. F. V. Time-averaged quantum dynamics and the validity of the effective Hamiltonian model. *Phys. Rev. A* **82**, 052106 (2010). URL https://link.aps.org/doi/10.1103/PhysRevA.82.052106.

[2] Qin, W. *et al.* Exponentially Enhanced Light-Matter Interaction, Cooperativities, and Steady-State Entanglement Using Parametric Amplification. *Phys. Rev. Lett.* **120**, 093601 (2018). URL https://link.aps.org/doi/10.1103/PhysRevLett.120.093601.

[3] Sazonova, V. *et al.* A tunable carbon nanotube electromechanical oscillator. *Nature (London)* **431**, 284 (2004). URL http://dx.doi.org/10.1038/nature02905.

[4] Üstünel, H., Roundy, D. & Arias, T. A. Modeling a suspended nanotube oscillator. *Nano Lett.* **5**, 523–526 (2005). URL https://doi.org/10.1021/nl0481371.

[5] Garcia-Sanchez, D. *et al.* Mechanical Detection of Carbon Nanotube Resonator Vibrations. *Phys. Rev. Lett.* **99**, 085501 (2007). URL https://link.aps.org/doi/10.1103/PhysRevLett.99.085501.

[6] Ning, Z. Y. *et al.* Transversally and axially tunable carbon nanotube resonators in situ fabricated and studied inside a scanning electron microscope. *Nano Lett.* **14**, 1221–1227 (2014). URL https://doi.org/10.1021/nl4040913.

[7] Truax, S., Lee, S.-W., Muoth, M. & Hierold, C. Axially tunable carbon nanotube resonators using co-integrated microactuators. *Nano Lett.* **14**, 6092–6096 (2014). URL https://doi.org/10.1021/nl501853w.

[8] Tsioutsios, I., Tavernarakis, A., Osmond, J., Verlot, P. & Bachtold, A. Real-time measurement of nanotube resonator fluctuations in an electron microscope. *Nano Lett.* **17**, 1748–1755 (2017). URL https://doi.org/10.1021/acs.nanolett.6b05065.

[9] Liu, D. E. Sensing kondo correlations in a suspended carbon nanotube mechanical resonator with spin-orbit coupling. *Quantum Engineering* **1**, e10 (2019). URL https://onlinelibrary.wiley.com/doi/full/10.1002/que2.10.

[10] Chaves, R., Lemos, G. B. & Pienaar, J. Causal Modeling the Delayed-Choice Experiment. *Phys. Rev. Lett.* **120**, 190401 (2018). URL https://link.aps.org/doi/10.1103/PhysRevLett.120.190401.

[11] Huang, H.-L. *et al.* A loophole-free Wheeler-delayed-choice experiment. *arXiv preprint arXiv:1806.00156* (2018). URL https://arxiv.org/abs/1806.00156.

[12] Polino, E. *et al.* Device independent certification of a quantum delayed choice experiment. *arXiv preprint arXiv:1806.00211* (2018). URL https://arxiv.org/abs/1806.00211.

[13] Yu, S. *et al.* Experimental realization of causality-assisted Wheeler's delayed-choice experiment using single photons. *arXiv preprint arXiv:1806.03689* (2018). URL https://arxiv.org/abs/1806.03689.

[14] Peruzzo, A., Shadbolt, P., Brunner, N., Popescu, S. & O'Brien, J. L. A Quantum Delayed-Choice Experiment. *Science* **338**, 634–637 (2012). URL http://science.sciencemag.org/content/338/6107/634.

[15] Kaiser, F., Coudreau, T., Milman, P., Ostrowsky, D. B. & Tanzilli, S. Entanglement-Enabled Delayed-Choice Experiment. *Science* **338**, 637–640 (2012). URL http://science.sciencemag.org/content/338/6107/637.

[16] Zheng, S.-B. *et al.* Quantum Delayed-Choice Experiment with a Beam Splitter in a Quantum Superposition. *Phys. Rev. Lett.* **115**, 260403 (2015). URL https://link.aps.org/doi/10.1103/PhysRevLett.115.260403.

[17] Liu, K. *et al.* A twofold quantum delayed-choice experiment in a superconducting circuit. *Sci. Adv.* **3**, e1603159 (2017). URL http://advances.sciencemag.org/content/3/5/e1603159.

[18] Huang, P. *et al.* Observation of an anomalous decoherence effect in a quantum bath at room temperature. *Nat. Commun.* **2**, 570 (2011). URL http://dx.doi.org/10.1038/ncomms1579.

[19] Lillie, S. E. *et al.* Environmentally Mediated Coherent Control of a Spin Qubit in Diamond. *Phys. Rev. Lett.* **118**, 167204 (2017). URL https://link.aps.org/doi/10.1103/PhysRevLett.118.167204.

[20] Xing, J. *et al.* Experimental investigation of quantum entropic uncertainty relations for multiple measurements in pure diamond. *Sci. Rep.* **7**, 2563 (2017). URL https://doi.org/10.1038/s41598-017-02424-6.

[21] Balasubramanian, G. *et al.* Ultralong spin coherence time in isotopically engineered diamond. *Nat. Mater.* **8**, 383–387 (2009). URL http://dx.doi.org/10.1038/nmat2420.

[22] Bar-Gill, N., Pham, L. M., Jarmola, A., Budker, D. & Walsworth, R. L. Solid-state electronic spin coherence time approaching one second. *Nat. Commun.* **4**, 1743 (2013). URL http://dx.doi.org/10.1038/ncomms2771.

[23] Moser, J., Eichler, A., Güttinger, J., Dykman, M. I. & Bachtold, A. Nanotube mechanical resonators with quality factors of up to 5 million. *Nat. Nanotechnol.* **9**, 1007–1011 (2014). URL http://dx.doi.org/10.1038/nnano.2014.234.

[24] Johansson, J. R., Nation, P. D. & Nori, F. Qutip: An open-source Python framework for the dynamics of open quantum systems. *Comput. Phys. Commun.* **183**, 1760–1772 (2012). URL http://www.sciencedirect.com/science/article/pii/S0010465512000835.

[25] Johansson, J. R., Nation, P. D. & Nori, F. Qutip 2: A Python framework for the dynamics of open quantum systems. *Comput. Phys. Commun.* **184**, 1234–1240 (2013). URL http://www.sciencedirect.com/science/article/pii/S0010465512003955.